GEOMATICS AND ENVIRONMENTAL ENGINEERING • Volume 17 • Number 3 • 2023

https://doi.org/10.7494/geom.2023.17.3.61

Salem Morsy[1], Shaker Ahmed[2]

Monitoring of Land Surface Temperature from Landsat Imagery: A Case Study of Al-Anbar Governorate in Iraq

Abstract: Land surface temperature (LST) estimation is a crucial topic for many applications related to climate, land cover, and hydrology. In this research, LST estimation and monitoring of the main part of Al-Anbar Governorate in Iraq is presented using Landsat imagery from five years (2005, 2010, 2015, 2016 and 2020). Images of the years 2005 and 2010 were captured by Landsat 5 (TM) and the others were captured by Landsat 8 (OLI/TIRS). The Single Channel Algorithm was applied to retrieve the LST from Landsat 5 and Landsat 8 images. Moreover, the land use/land cover (LULC) maps were developed for the five years using the maximum likelihood classifier. The difference in the LST and normalized difference vegetation index (NDVI) values over this period was observed due to the changes in LULC. Finally, a regression analysis was conducted to model the relationship between the LST and NDVI. The results showed that the highest LST of the study area was recorded in 2016 (min = 21.1°C, max = 53.2°C and mean = 40.8°C). This was attributed to the fact that many people were displaced and had left their agricultural fields. Therefore, thousands of hectares of land which had previously been green land became desertified. This conclusion was supported by comparing the agricultural land areas registered throughout the presented years. The polynomial regression analysis of LST and NDVI revealed a better coefficient of determination (R^2) than the linear regression analysis with an average R^2 of 0.423.

Keywords: land surface temperature, Landsat, single channel algorithm, NDVI, land use/land cover, classification, regression

Received: 29 April 2022; accepted: 13 January 2023

[1] Cairo University, Faculty of Engineering, Public Works Department, Giza, Egypt, email: smorsy@eng.cu.edu.eg, https://orcid.org/0000-0002-1683-2050

[2] Cairo University, Faculty of Engineering, Public Works Department, Giza, Egypt; University of Anbar, College of Engineering, Department of Civil Engineering, Ramadi, Iraq, email: shakerfaahad@uoanbar.edu.iq

1. Introduction

Thermal remote sensing primarily records the emitted radiation from the ground to extract the surface temperature. Land surface temperature (LST) is the estimated temperature of the ground cover, such as soil surface temperature for bare soil, and canopy surface temperature for vegetated areas. LST plays an important role in many studies, such as hydrological projects, climate change, land use/land cover (LULC), and soil moisture [1, 2]. Landsat satellites provide the data for LST retrieval through the Thematic Mapper (TM) onboard Landsat 5, Enhanced Thematic Mapper Plus (ETM+) onboard Landsat 7 or Operational Land Imager/Thermal Infrared Sensor (OLI/TIRS) onboard Landsat 8 [3].

Several algorithms have been proposed to estimate LST from satellite images, such as mono window algorithm (MW), single channel algorithm (SC), radiative transfer equation (RTE) and split window algorithm (SW) [2–4]. The MW was originally developed by [5]. This method requires three special parameters, namely land surface emissivity (LSE), atmospheric transmittance, and the effective mean atmospheric temperature. The method was improved by [6] tZo be appropriate for Landsat 8. The SC was first presented by [7] and then improved by [8] to estimate LST from Landsat thermal infrared data. The RTE was initially proposed by [9], who estimated sea surface temperature depending on the difference in atmospheric absorption of two adjacent Long Wavelength InfraRed bands. Price [10] implemented SW for LST extraction from Advanced Very High Resolution Radiometer (AVHRR) sensor data. Thereafter, researchers have applied and improved the SW for several purposes [1].

The main differences between these methods are in the mathematical model employed and the input parameters [3]. Although the MW and SC are sensitive to the error of atmospheric water vapor content, the MW is very sensitive to the error of the effective mean atmospheric temperature [4]. This is due to the fact that it needs near-surface air temperature, unlike other algorithms, to calculate the effective mean atmospheric temperature [3]. The SC and RTE are found to be consistent if spatial-temporal changes are considered, meaning that they present close results regardless of the season [3]. The SW is only applicable on Landsat 8 as it requires two TIR bands. Therefore, the SC is considered in this research.

The importance of LST for environmental studies has been highlighted by several authors. Kumar Thakur and Gosavi [1] studied the downstream part of the Sainj River of the Indian Himalayan Region, wherein changes in LST of the area over sixteen years were observed. The LST was extracted using the SC from Landsat 7 (ETM+) for October 2001, and using the SW from Landsat 8 (OLI/TIRS) for October 2016. Sekertekin and Bonafoni [3] performed a comprehensive analysis of the three LST retrieval algorithms (RTE, SC and MW) using Landsat 5, 7 and 8 imagery data, and additionally, the SWA was assessed for Landsat 8 imagery data. Morsy and Hadi [11] studied the change of LST from Landsat 8 over different LULC

and their relationship with spectral indices. The SC has been widely applied to estimate LST from Landsat imagery because of its simplicity and because it only requires one thermal band [12]. It can also be applied to different thermal sensors with similar equations but with different coefficients [7, 13].

The impact of LULC on the LST has been studied using multi-spectral/multi-temporal satellite images [14–17]. For instance, Pal and Ziaul [14] used Landsat 5 and Landsat 8 images of 1991, 2010 and 2014 to estimate the LST of the English Bazar Municipality in India. The results showed that the LST increased by about 0.070°C/year during winter and 0.114°C/year during summer. The relation between LST against Normalized Difference Vegetation Index (NDVI) and Normalized Difference Built-up Index was modelled using linear regression. In another piece of research by [15], the relationship between LST and main LULC types (vegetation, man-made features, cropland) of an inner-city area of Hanoi in Vietnam was studied. The analysis of Landsat images of years 2003, 2007 and 2015 showed a non-linear relationship between LULC and LST. Therefore, the relationship between LST and spectral indices might be linear or non-linear.

Hidalgo-García and Arco-Díaz [16] studied the metropolitan area of the city of Granada in Spain using Landsat images from 1985 to 2020. An average increase of LST by 2.2°C was reported as a result of increases in built-up and bare soil coverage as well as a decrease in water bodies, vegetation, and farmland coverage. Ahmed [17] used ASTER with Landsat images from 1988 to 2014 to estimate LST of Suez Governorate in Egypt. Over 26 years, LULC changes had a significant impact on increasing LST of different covers. The LST was increased by 4.5°C, 2°C and 7.5°C for urban, vegetated areas and reclaimed areas, respectively.

Al-Ruzouq et al. [18] estimated the LST over coastal cities in the United Arab Emirates using Landsat and MODIS images from 2000 to 2020. The LST was estimated for daytime and nighttime during the summer and winter seasons. Unlike other studies, the daytime LST did not increase significantly during either summer or winter seasons. On the other hand, the nighttime LST has increased by about 17% since 2000. This could be attributed to the fact that the bare land desert was replaced by vegetation, high-rise buildings, and industrial activities as reported in [18]. This study proved that the relation between LULC and LST relies on the season and daytime of the study. Similarly, Majumder et al. [19] analyzed Landsat images of three cities in Punjab, India during winter and summer for 1991, 2001, 2011, and 2018, while Amindin et al. [20] reported a 2.5°C average increase of LST over 21 years in different seasons in Ahvaz, Iran.

As a result, LST monitoring using multi-spectral/multi-temporal satellite images is subject to the study area (i.e., LULC type, geographic location and season of data acquired). Therefore, the purpose of this study is to retrieve and monitor the LST of the main part of Al-Anbar Governorate in Iraq from Landsat imagery of five years (2005, 2010, 2015, 2016 and 2020) using the SC. In addition, the relation of the LST against the NDVI values and different LULC over the five years are

presented. The rest of this paper is structured as following. Section 2 describes the study area and datasets. The LST retrieval procedures and images classification are explained in Section 3. The results and discussion are illustrated in Section 4. Section 5 presents the conclusions of this research.

2. Study Area and Datasets

The study area is located in Al-Anbar Governorate, the western part of Iraq, as shown in Figure 1.

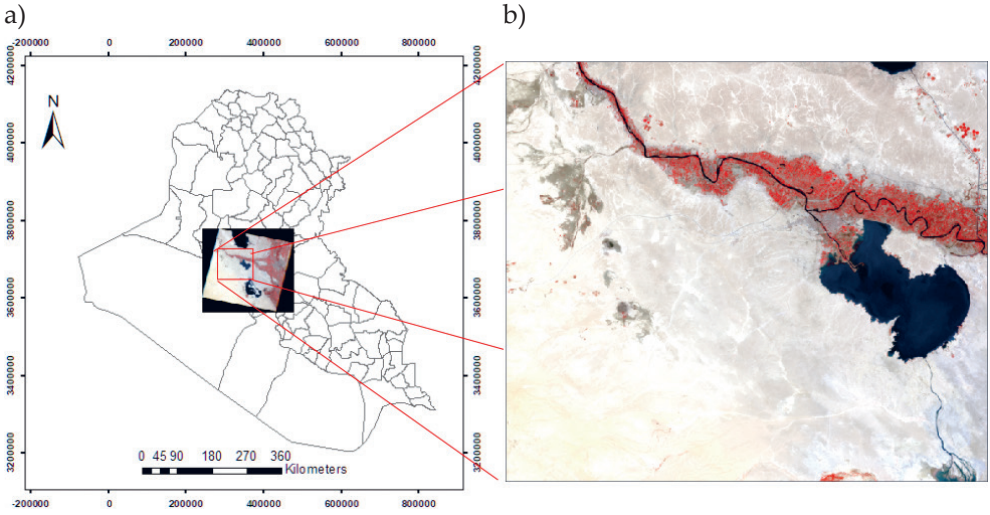

Fig. 1. The study area: Iraq map (a)
and a subset of a Landsat image covering the study area (b)

Al-Anbar is the largest Governorate in Iraq with an area of about 138,501 km^2. It lies between longitude of 38°47′E to 44°17′E and between latitude of 30°24′N to 35°11′N. It shares borders with Syria, Jordan, and Saudi Arabia. The average elevation of this area is about 45 m above mean sea level. The area of study region is about 7,175 km^2 with dimensions of 90.81 km × 79.02 km. The study region consists of urban and agricultural areas. The urban areas are distributed between residential and commercial uses and extend along the main road linking Baghdad and the Al-Anbar Governorate. The region is bordered by the Euphrates River, and there is a network of secondary roads linking its parts to each other. Its climate is characterized by hot and dry summers, cold and rainy winters, and summer temperatures sometimes reach 50°C. In this region, the urban areas expanded illegally and many agricultural areas were also destroyed as a result of military operations during the

2016 war. These developments led to changes in the climate of this region and its natural environment.

The satellite images of study area were downloaded from the USGS website https://earthexplorer.usgs.gov/. Several images were visually investigated in the early stage of this study from 1990 to 2020. Five cloud free images were selected at years of 2005, 2010, 2015, 2016 and 2020 to represent the change in the last twenty years as shown in Table 1. The images were downloaded directly from the USGS with UTM_WGS84_Zone38N and 30 m resolution. All of the images were acquired in the early morning about 7:30 am under a clear sky. The images were of the level terrain precision correction type (L1TP). Thus, they were already radiometrically calibrated and orthorectified using ground control points and digital elevation model data to correct for relief displacement (https://www.usgs.gov/landsat-missions/landsat-collection-1). The images were then atmospherically corrected using the dark-object subtraction function embedded in ENVI 5.3 software package. After that, the layer stacking tool was used to combine the single-band images into multi-band images. Finally, the images were clipped to cover the study area. Figure 2 shows the false color composite of Landsat images of the five years used in this research.

Table 1. The selected images (30 m resolution) for the study area

Satellite / sensor	Path / row	No. of bands	Acquisition date	Passage time [hr: min: sec]
Landsat 5 / TM	169/37	7	6-APR-2005	07: 26: 54.3120940
Landsat 5 / TM	169/37	7	20-APR-2010	07: 30: 40.3340940
Landsat 8/ OLI/TIRS	169/37	11	18-APR-2015	07: 39: 11.0493140
Landsat 8/ OLI/TIRS	169/37	11	20-APR-2016	07: 39: 20.9950870
Landsat 8/ OLI/TIRS	169/37	11	15-APR-2020	07: 39: 24.1696039

Landsat 5 TM sensor has six reflective bands (visible, near-infrared, and short-wavelength infrared) with a spatial resolution of 30 m, and one band in the thermal region (band 6). The thermal band has a spatial resolution of 120 m, but it can be downloaded directly with a spatial resolution of 30 m from the USGS. The Landsat 8 OLI sensor has nine reflective bands and two bands in the TIRS region (band 10 and band 11). The reflective bands have a spatial resolution of 30 m, while thermal bands have a 100 m native spatial resolution but they are resampled and published with 30 m by the USGS.

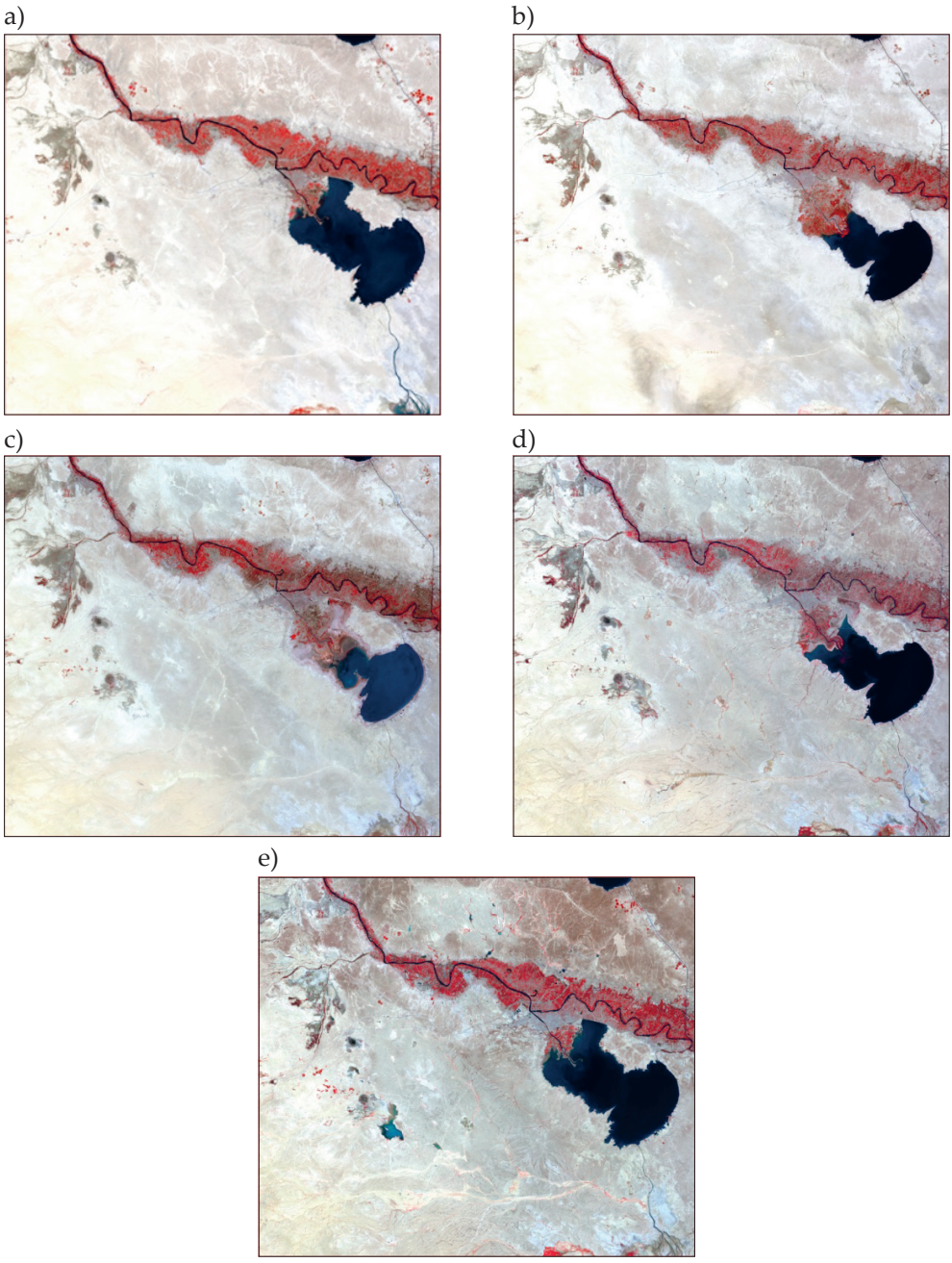

Fig. 2. False color composite of Landsat 5 for 2005 (a) and 2010 (b) visualized as band 4 (near infrared), band 3 (red) and band 2 (green) in RGB layers, and Landsat 8 for 2015 (c), 2016 (d) and 2020 (e) visualized as band 5 (near infrared), band 4 (red) and band 3 in RGB layers

3. Methodology

3.1. LST Retrieval from Landsat Imagery

In this study, the SC was used for LST retrieval from the Landsat satellite images. Band 6 (thermal) and band 10 (TIRS) were used for LST estimation from Landsat 5 and Landsat 8 images, respectively. The NDVI, and hence LSE were calculated using band 3 (red) and band 4 (NIR) from Landsat 5, and band 4 (red) and band 5 (NIR) from Landsat 8. The workflow of this research is illustrated in Figure 3. The steps of calculating the LST from Landsat 5 and Landsat 8 images are as follows.

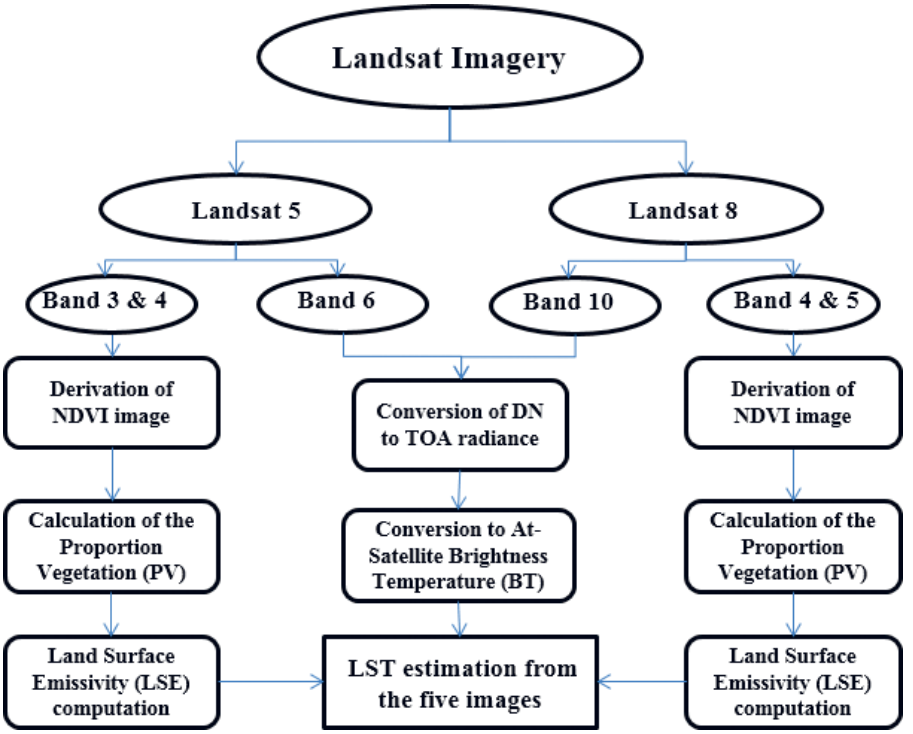

Fig. 3. LST retrieval workflow

Conversion of DN to spectral/TOA radiation (L_λ)

The procedures of LST estimation from Landsat 5 images are slightly different from those for Landsat 8 images. The digital number (DN) of the thermal band was used to compute spectral radiation (L_λ) for Landsat 5 as provided in Equation (1) [21] and top of atmosphere (TOA) radiation for Landsat 8 as provided in Equation (2) [22]. All of the parameters used in calculations can be obtained from the metadata file available with the images (Tab. 2).

$$L_{\lambda} = \frac{L_{\max\lambda} - L_{\min\lambda}}{Q_{cal\max} - Q_{cal\min}} \cdot (Q_{cal} - Q_{cal\min}) + L_{\min\lambda} \quad (1)$$

where:

L_{λ} – the spectral radiation,
Q_{cal} – the image value (DN),
$Q_{cal\min}$ – the minimum DN corresponding to $L_{\min\lambda}$, $Q_{cal\min} = 1$,
$Q_{cal\max}$ – the maximum DN corresponding to $L_{\max\lambda}$, $Q_{cal\max} = 255$,
$L_{\min\lambda}$ – at-sensor radiation scaled to $Q_{cal\min}$ [W·m^{-2}·sr^{-1}·μm^{-1}],
$L_{\max\lambda}$ – at-sensor radiation scaled to $Q_{cal\max}$ [W·m^{-2}·sr^{-1}·μm^{-1}].

$$L_{\lambda} = M_L \cdot Q_{cal} + A_L \quad (2)$$

where:

M_L – band specific multiplicative rescaling factor,
A_L – band specific additive rescaling factor.

Conversion of DN to at-satellite brightness temperature

This step was applied to convert the spectral radiation to brightness temperature (BT) using Planck's inverse function and the thermal constants provided in the metadata (Tab. 2) as provided in Equation (3) [8].

$$\mathrm{BT} = \frac{K_2}{\ln\left(\frac{K_1}{L_{\lambda}} + 1\right)} - 273.15 \quad (3)$$

where:

BT – brightness temperature [°C],
K_1, K_2 – the calibration constants.

Table 2. Landsat calibration parameters

Parameter	Landsat 5 (band 6)	Landsat 8 (band 10)
K_1	607.76	774.89
K_2	1260.56	1321.08
M_L	–	3.34E-04
A_L	–	0.10
$L_{\min\lambda}$	1.238	–
$L_{\max\lambda}$	15.303	–

Land surface emissivity (LSE) computation

Surface emissivity refers to the ability of the surface to transform heat energy into radiant energy. LSE is one of the parameters to retrieve accurate LST from remotely sensed imagery [7]. LSE depends on the proportion of vegetation (PV), which in turn depends on NDVI. Calculations of LSE, PV and NDVI are as follows [21]:

$$\mathrm{LSE} = 0.0004 \cdot \mathrm{PV} + 0.986 \tag{4}$$

$$\mathrm{PV} = \left[\frac{\mathrm{NDVI} - \mathrm{NDVI}_{\min}}{\mathrm{NDVI}_{\max} - \mathrm{NDVI}_{\min}} \right]^2 \tag{5}$$

$$\mathrm{NDVI} = \frac{\mathrm{NIR} - Red}{\mathrm{NIR} + Red} \tag{6}$$

The NDVI was first defined by [23] as in Equation (6). The basic idea of the NDVI is that the chlorophyll in green plants absorbs red radiation, while the near-infrared (NIR) radiation is reflected or scattered. As a result, vegetation has high NDVI values. Theoretically, NDVI ranges from −1 to 1, while the observed range is usually smaller, with value around 0 for bare soil (low or no vegetation), and value of 0.9 or larger for dense vegetation [24]. In this study, the NDVIs were derived directly from the Landsat imageries as illustrated in Figure 3.

Land surface temperature (LST) retrieval

Brightness temperature can be converted to LST using Equation (7):

$$\mathrm{LST} = \frac{\mathrm{BT}}{1 + \left(\lambda \cdot \frac{\mathrm{BT}}{P} \right) \cdot \ln \mathrm{LSE}} \tag{7}$$

where:

LST – land surface temperature,
λ – the wavelength of the emitted radiance,
P – $P = h \cdot C/S$ ($P = 1.438 \cdot 10^{-2}$ m·K)
S – Boltzmann's constant ($S = 1.38 \cdot 10^{-23}$ J·K^{-1}),
h – Planck's constant ($h = 6.626 \cdot 10^{-34}$ J·s),
C – velocity of light ($C = 2.998 \cdot 10^{8}$ m·s^{-1}),
LSE – the spectral emissivity.

3.2. LST Validation

The best way to validate the results is to compare the retrieved LST with in situ measurements of temperatures (i.e., ground truth). However, it is extremely difficult to carry out such measurements and it is not feasible for the study of past surface temperatures if data were not already collected at the evaluated time [4, 6]. Similarly, due to dynamic nature of LST, both spatially and temporally, it was impossible to get ground-based values to validate the LST in this research. Previous studies have usually used simulated data when proposing a new algorithm or modification of an existing algorithm [2, 6, 12]. However, the atmospheric parameters and the LSE are difficult to obtain, and the simulation process is complicated [4]. Alternatively, we compared the retrieved LST with MODIS LST products similar to the study by Kumar Thakur and Gosavi [1], since MODIS surface temperature products are free and easy to obtain.

3.3. LULC Classification

The LULC classification of the study area from the five images was conducted using a widely used supervised classification method, the maximum likelihood classifier (MLC). MLC assigns pixels to the class with the principal of highest likelihood. Class mean and covariance matrix are the main inputs to the function and can be extracted from the training pixels of a special class [25]. The study area was classified into four types, including urban areas, vegetation areas, water, and open land. The overall accuracy and kappa statistics were calculated using 300 check points to test the performance of the classification process. The check points were randomly distributed over the satellite images and the classified images. By means of the visualization and interpretation of the satellite images, each point was manually assigned a class (i.e., urban areas, vegetation areas, water or open lands) and used as a reference point. Then, the confusion matric was computed for each year, whereas a comparison between the classified points and reference points was conducted. Finally, the overall accuracy and kappa statistics were calculated.

4. Results and Discussion

The LST and NDVIs were calculated from the five images for the study area as shown in Figures 4 and 5, respectively. The summary of the minimum, maximum, mean and standard deviation (SD) of LST as well as NDVIs of the five images is listed in Table 3.

The highest LST values were recorded in the year 2016, whereas the spatial distribution of LST in this year ranged from a minimum of 21.1°C to a maximum of 53.2°C with a mean of 40.8°C and SD of 4.2°C. This is attributed to the change of LULC as the effect of the war in this year.

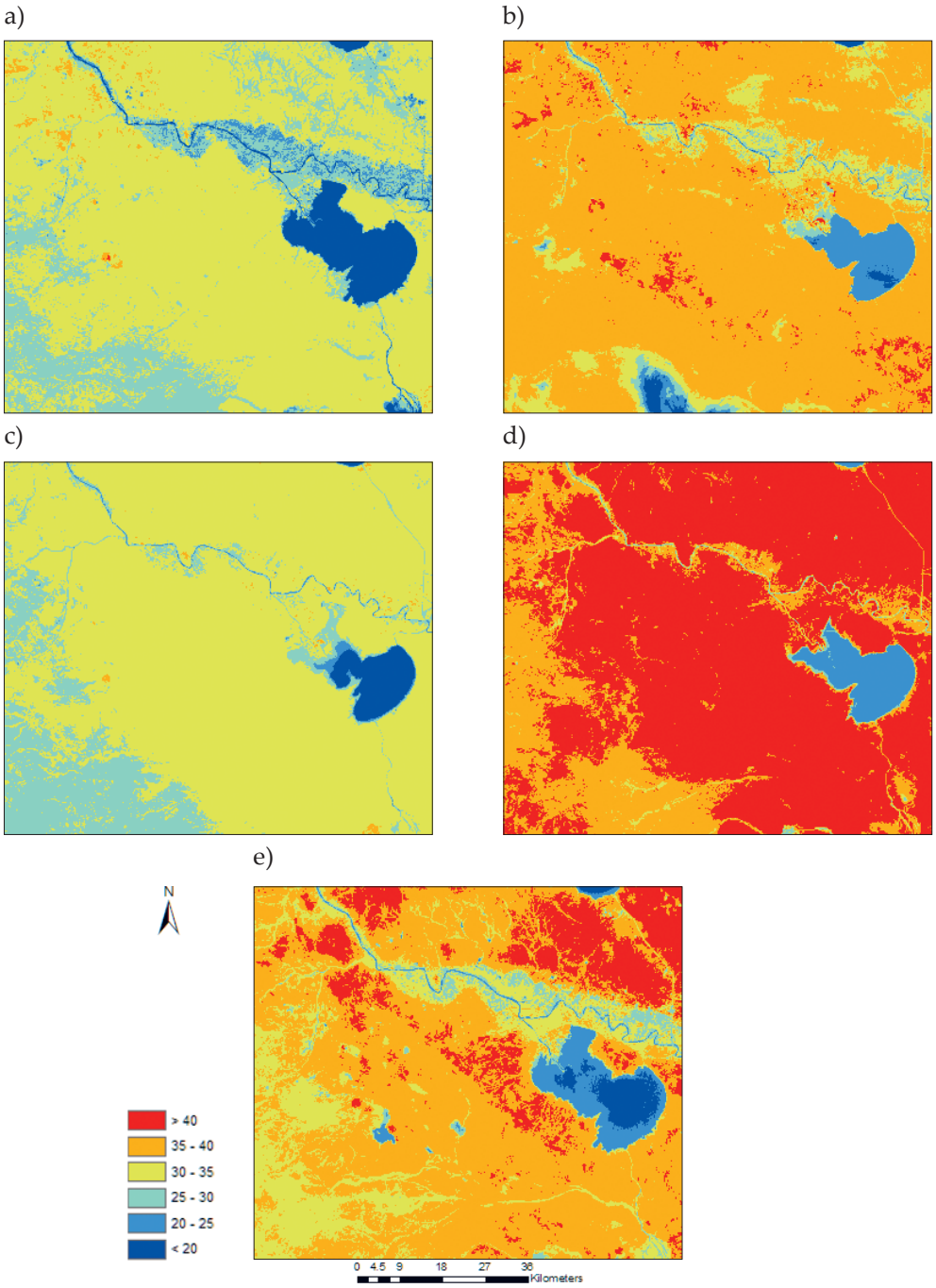

Fig. 4. LST of the study area
for 2005 (a), 2010 (b), 2015 (c), 2016 (d) and 2020 (e)

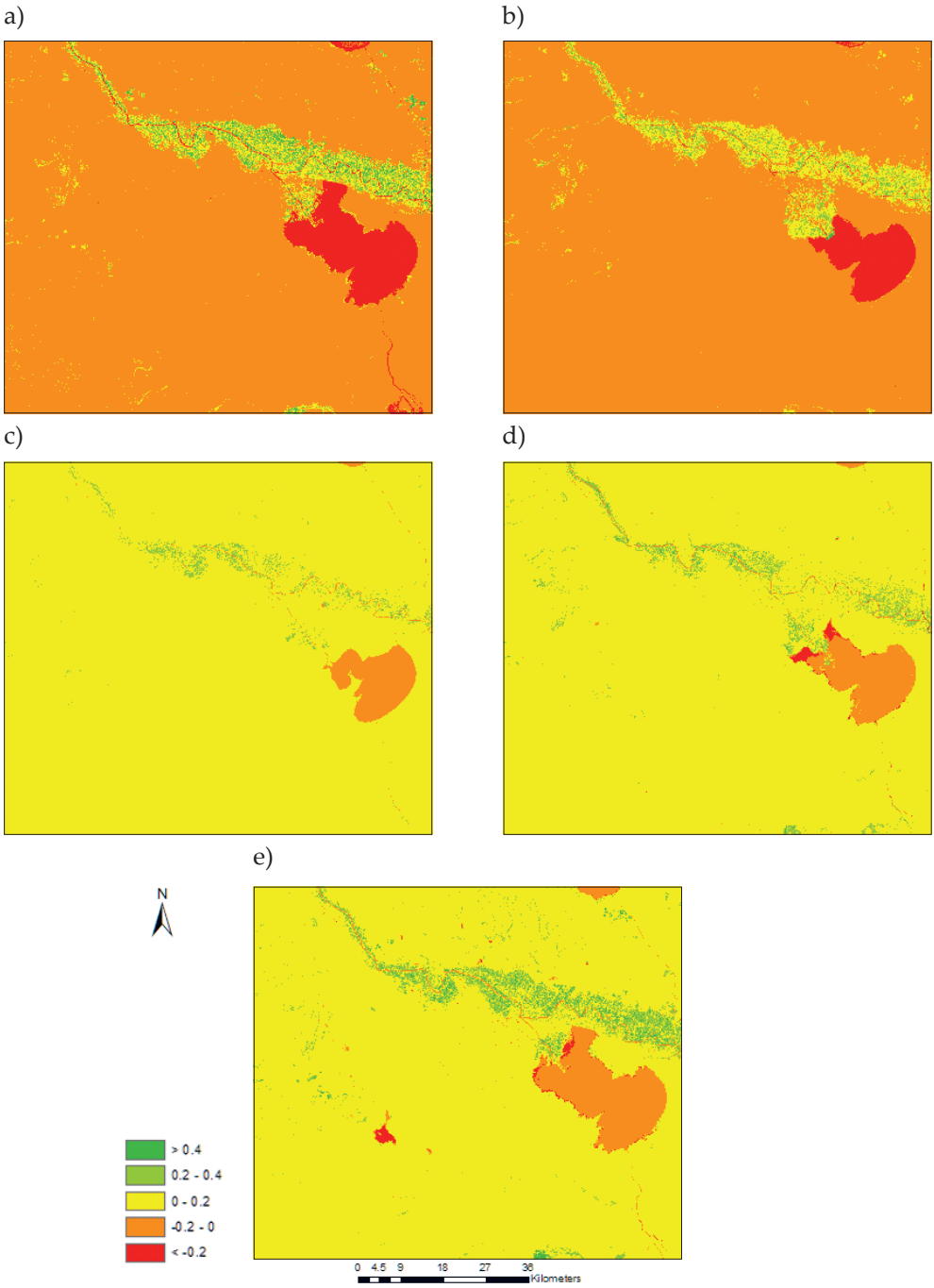

Fig. 5. NDVI of the study area
for 2005 (a), 2010 (b), 2015 (c), 2016 (d) and 2020 (e)

The NDVI is an essential index in LST estimation from Landsat images as well as being used in this research to monitor the healthy vegetative condition. The highest values of NDVI were recorded for the year 2005 ranging from −0.58 (min) to 0.71 (max), while the lowest values were recorded for the year 2015 ranging from −0.20 (min) to 0.49 (max). Despite the highest LST in 2016, the NDVI values for this year ranged from −0.36 (min) to 0.60 (max).

Table 3. Summary of LST and NDVI for the five years

Image year	LST [°C]				NDVI			
	min	max	mean	SD	min	max	mean	SD
2005	13.3	41.5	30.0	3.9	−0.58	0.71	−0.03	0.11
2010	18.5	48.1	36.3	4.1	−0.44	0.55	−0.04	0.07
2015	17.3	39.8	31.2	2.5	−0.20	0.49	0.07	0.04
2016	21.1	53.2	40.8	4.2	−0.36	0.60	0.09	0.05
2020	18.5	48.5	35.9	4.9	−0.35	0.62	0.09	0.07

We used standard datasets of MODIS LST products to validate the LST retrieved for Landsat 5 and 8. The MODIS datasets were downloaded from the MODIS products website https://lpdaac.usgs.gov/products/mod11a1v006/. MODIS LST products of the five years were projected to UTM_WGS84_Zone38N, clipped for the study area, and converted from Kelvin to Celsius. Table 4 provides the statistics of MODIS LST and the difference between the retrieved LST from Landsat images and MODIS LST. The results showed that the MODIS LST was close to the LST retrieved from Landsat 5 and 8. It should be kept in mind that the MODIS LST is of a coarser spatial resolution of 1 km, while Landsat is 30 m. The average error of the minimum, maximum, mean and SD was 1.7, 1.8, 6.6 and 0.7°C, respectively. In general, the same tradeoff of hot and cold spots was observed in MODIS LST outputs with comparatively good estimates of high and low LST values.

Table 4. MODIS LST statistics compared with Landsat LST

Image year	MODIS LST [°C]				LST [°C] difference (MODIS-Landsat)			
	min	max	mean	SD	min	max	mean	SD
2005	16.7	45.4	38.1	5.2	3.4	3.9	8.1	1.3
2010	18.0	51.7	46.4	5.0	−0.5	3.6	10.1	0.9
2015	17.4	39.4	34.2	3.1	0.1	−0.4	3.0	0.6
2016	24.6	54.7	47.1	4.7	3.5	1.5	6.3	0.5
2020	20.4	49.1	41.2	5.3	1.9	0.6	5.3	0.4

Regression analysis was carried out to model the relationship between the LST and NDVI over the five years. Linear and polynomial regression models were applied for the LST against NDVI as shown in Figure 6.

The results of the regression models indicated a negative correlation between LST and NDVI. The relationship was compatible with previous studies of [14, 15]. The linear regression revealed low R^2 with a maximum value of 0.108 in 2010. Polynomial regression models, on the other hand, were carried out and the results showed a higher coefficient of determination (R^2) ranged from 0.242 to 0.612. Thus, the relationship is not always a linear and could be non-linear as reported by Tran et al. [15]. The lower R^2 (i.e., 0.242) was in 2016, when many people were displaced and left their agricultural fields.

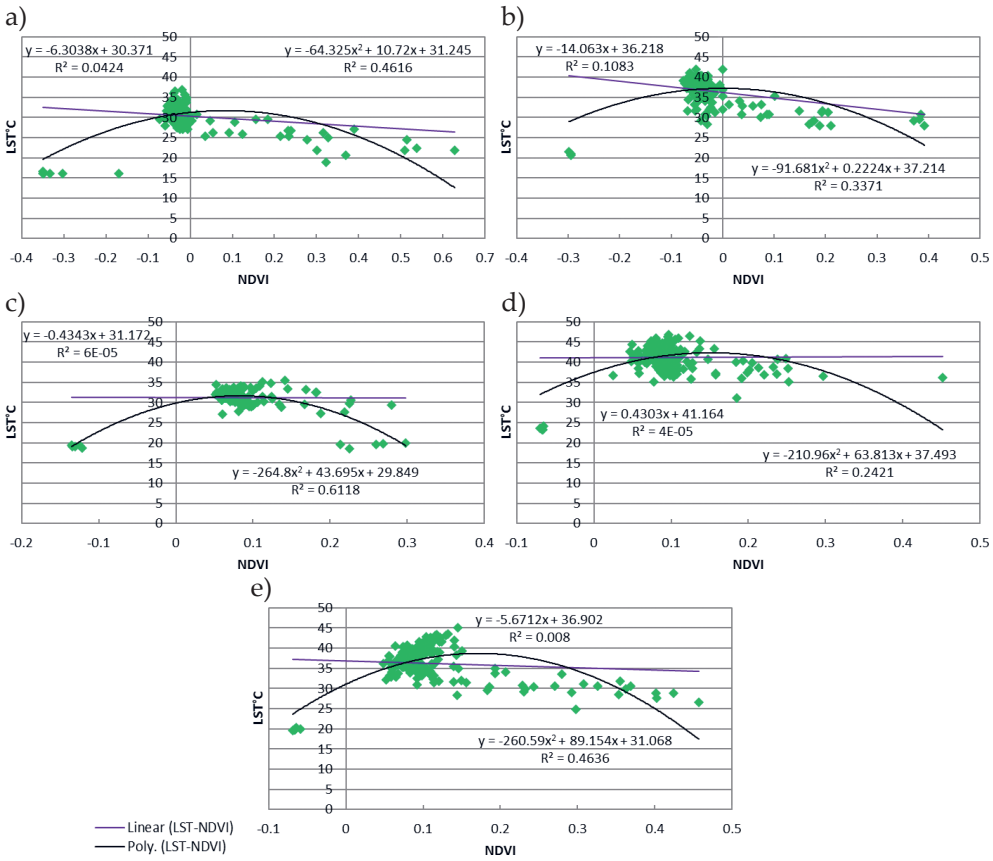

Fig. 6. Regression relationship between LST and NDVI for 2005 (a), 2010 (b), 2015 (c), 2016 (d) and 2020 (e)

The corresponding LULC change was also studied to interpret the effect of land use changes on the values of LST. The study area was classified into four classes, namely vegetation, urban, water, and open land using MLC embedded in the ERDAS IMAGINE 2015 software package. Figure 7 shows the LULC of the different years of study. The classified images were compared with the actual LULC for the five years using the same 300 check points as aforementioned.

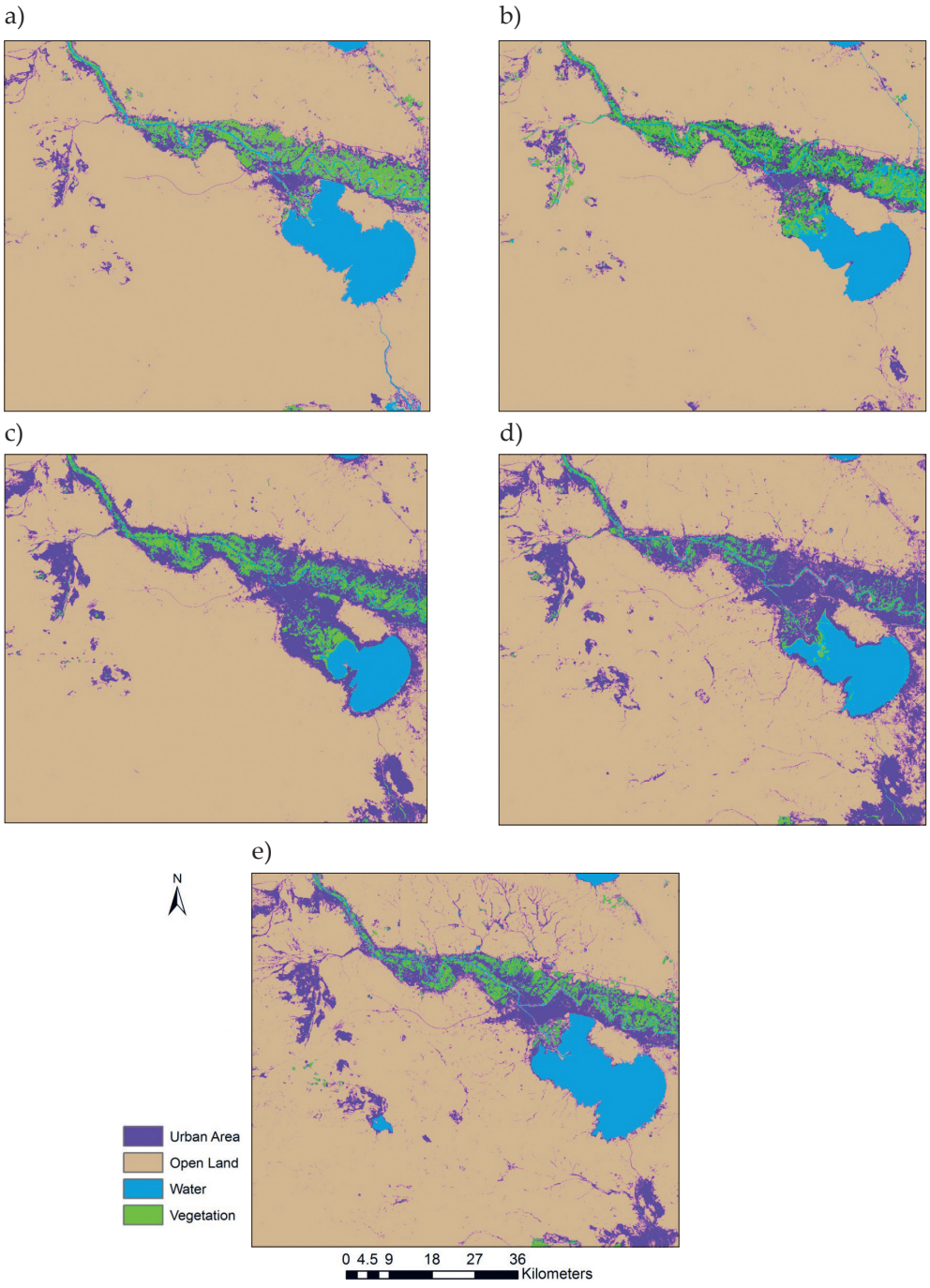

Fig. 7. LULC for 2005 (a), 2010 (b), 2015 (c), 2016 (d) and 2020 (e)

The confusion matrices were then derived and the overall classification accuracy as well as overall kappa statistics was calculated as listed in Table 5. Results showed an average overall accuracy and kappa statistics of 86.67% and 0.827, respectively.

Table 5. Accuracy assessment of the five classified images

Image year	Overall accuracy [%]	Kappa statistics
2005	86.67	0.822
2010	88.33	0.844
2015	85.00	0.800
2016	85.00	0.800
2020	88.33	0.867

The LST statistics for each LULC were extracted and are summarized in Figure 8. It was observed that the lowest temperatures were associated with water and vegetation areas, while the highest temperatures were associated with urban and open land areas. Thus, replacing natural areas as water and vegetation with non-evaporating and non-transpiring surfaces (e.g., urban areas) raised the temperature of the environment.

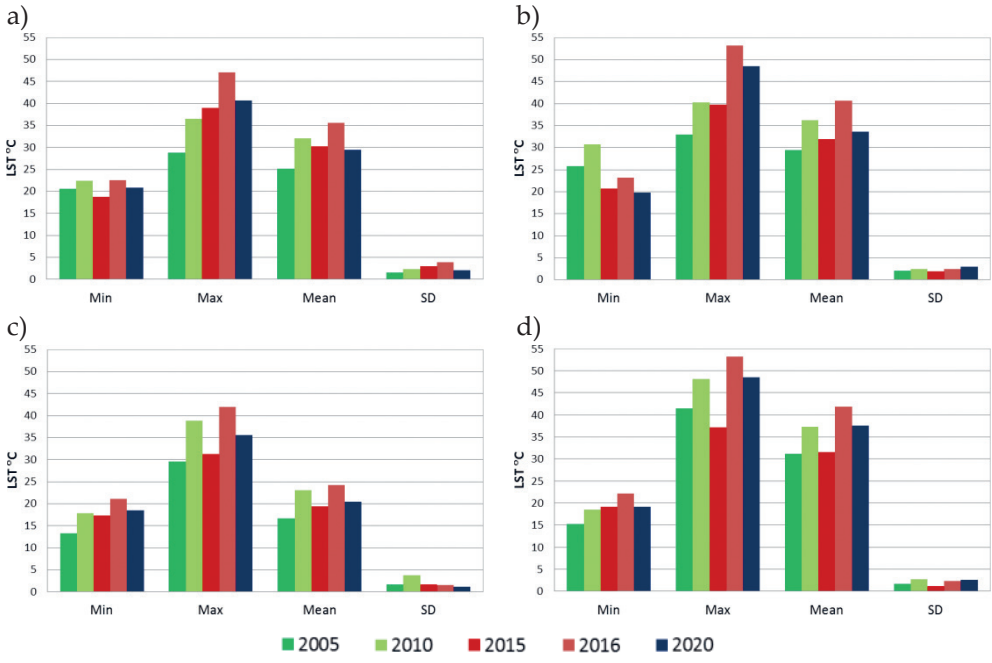

Fig. 8. LST statistics of LULC of the five years
for vegetation (a), urban (b), water (c), and open land (d)

Finally, the areas in square kilometers of the four classes were calculated in order to relate these areas with the LST values. Table 6 provides the areas of different classes in the study area. The change in LULC areas were studied for the period from 2005 and 2020.

Table 6. Areas of land classes

Image year	Area of class [km^2]			
	vegetation	urban	water	open land
2005	213.72	388.62	431.61	6141.85
2010	276.94	400.99	343.69	6154.20
2015	255.07	943.57	206.57	5770.60
2016	134.57	1066.48	283.98	5690.78
2020	215.86	798.82	402.34	5758.78

Generally, the open land class had the largest areas, representing more than 80% of the total study area, while vegetation had the smallest area with less than 4% of the total study area, regardless of the year of study. The water areas are different over years as they are lakes for storing water, and they are highly variable because of their connection to rivers. In addition, they are closely related to the amount of rainfall, which obviously varies from year to year. It was also observed that the urban area increased from 386.54 km^2 in 2005 to 1066.48 km^2 in 2016. Thus, a large expansion of 679.94 km^2 was noticed in built up area over the time period of eleven years. On the other hand, the smallest area of vegetation (134.57 km^2) was recorded during the year of the war (2016), as shown in Table 5.

The LST of 2010 increased as illustrated in Figure 4b. and statistics in Table 3. This was mainly due to the increase of open land and urban area as provided in Table 5. On the other hand, the LST of 2015 decreased compared to 2010 (Fig. 4c). This could be because of the significant increase of the urban areas, especially on the west side of the study area (Fig. 7c), and hence the shadows of building volumes (height and area) caused a cooling effect on the study area [26, 27]. In 2016, the LST increased, again due to the effect of war, as many people were displaced and left their agricultural fields. Therefore, thousands of hectares of land became desertified, having previously been green lands, and were classified as urban areas. Between 2016 and 2020, people were resettled and started cultivating their land again. Therefore, as for 2020, the vegetation area increased and the urban areas decreased.

In addition, we achieved good results of the retrieved LST compared to the results achieved in similar works that used SC for LST retrieval from Landsat images. Considering simulated data in comparison, the study of Wang et al. [6] revealed a root mean square error (RMSE) of −2.9°C, while Wang et al. [12] found 1.8°C RMSE. Other studies used in situ measurements in comparison. For instance, Sekertekin

and Bonafoni [3] demonstrated a RMSE of 2.7°C, while Wang et al. [4] demonstrated an average error and RMSE of 3.5°C and 0.7°C, respectively.

Concerning limitations of this study, it was deemed necessary that future research endeavors should evaluate different seasons for temporal monitoring. In addition, any future work should consider building volumes, shadows and their distribution in different seasons that could influence the LST. It should also be noted that a shortcoming in this case study was that the MODIS LST was used to assess the retrieving LST accuracy due to the lack of in situ LST data simultaneously available when the satellites passed. In future studies, in situ LST data could be measured with the same overpass of satellites for the calibration and validation of the LST distribution.

5. Conclusions

In this paper, Landsat 5 TM and Landsat 8 OLI/TIRS images were used to retrieve the LST of the main part of Al-Anbar Governorate for the years 2005, 2010, 2015, 2016 and 2020. The highest LST values were recorded in the year of 2016. The distribution of LST in this year ranged from 21.1°C to 53.2°C with a mean and SD of 40.8°C and 4.2°C, respectively. It should be pointed out that the highest rate of LST in this year is because of the reduction in vegetation area, which had become desertified and classified in our analysis as an urban area.

The LST is usually affected by the LULC type. Therefore, the LULC was developed for the five years based on MLC and revealed an average overall accuracy and kappa statistics of 86.67% and 0.827, respectively. Then, LST statistics for each individual class were analyzed. Within the study period, it was observed that the LST was at its highest in the urban areas, while the lowest LST was recorded in vegetation areas, especially palm groves scattered over the study area. Accordingly, the increase in urban growth and the decrease of agricultural areas has a direct and negative environmental impact, especially in areas related to high temperatures.

In addition, NDVIs were derived for the five years and their statistics were calculated. A negative relationship was observed between LST and NDVIs, which was supported by modelling the relationship between LST and NDVIs using linear and non-linear (i.e., polynomial) regression analysis. The results revealed higher R^2 for polynomial regression rather than linear regression with a max. R^2 of 0.612 in 2015.

Author Contributions

Author 1: conceptualization, methodology, software, investigation, data curation, visualization, writing – review and editing, supervision.

Author 2: conceptualization, methodology, software, validation, formal analysis, resources, data curation, writing – original draft preparation.

Acknowledgements

The authors would like to thank the editor and the anonymous reviewers for their valuable comments and suggestions which helped to improve this work.

References

[1] Kumar Thakur P., Gosavi V.E.: *Estimation of temporal land surface temperature using thermal remote sensing of Landsat-8 (OLI) and Landsat-7 (ETM+): A study in Sainj River Basin, Himachal Pradesh, India*. Environment & We an International Journal of Science & Technology, vol. 13, 2018, pp. 29–45.

[2] Jiménez-Muñoz J.C., Sobrino J.A., Skoković D., Mattar C., Cristóbal J.: *Land surface temperature retrieval methods from Landsat-8 thermal infrared sensor data.* IEEE Geoscience and Remote Sensing Letters, vol. 11(10), 2014, pp. 1840–1843. https://doi.org/10.1109/LGRS.2014.2312032.

[3] Sekertekin A., Bonafoni S.: *Land surface temperature retrieval from Landsat 5, 7, and 8 over rural areas: Assessment of different retrieval algorithms and emissivity models and toolbox implementation*. Remote Sensing, vol. 12(2), 2020, 294. https://doi.org/10.3390/rs12020294.

[4] Wang L., Lu Y., Yao Y.: *Comparison of three algorithms for the retrieval of land surface temperature from Landsat 8 images*. Sensors, vol. 19(22), 2019, 5049. https://doi.org/10.3390/s19225049.

[5] Qin Z., Karnieli A., Berliner P.: *A mono-window algorithm for retrieving land surface temperature from Landsat TM data and its application to the Israel-Egypt border region*. International Journal of Remote Sensing, vol. 22(18), 2001, pp. 3719–3746. https://doi.org/10.1080/01431160010006971.

[6] Wang F., Qin Z., Song C., Tu L., Karnieli A. Zhao S.*: An improved mono-window algorithm for land surface temperature retrieval from Landsat 8 thermal infrared sensor data*. Remote Sensing, vol. 7(4), 2015, pp. 4268–4289. https://doi.org/10.3390/rs70404268.

[7] Jiménez-Muñoz J.C., Sobrino J.A.: *A generalized single-channel method for retrieving land surface temperature from remote sensing data*. Journal of Geophysical Research: Atmospheres, vol. 108(D22), 2003, 4688. https://doi.org/10.1029/2003JD003480.

[8] Jiménez-Muñoz J.C., Sobrino J.A.: *A single-channel algorithm for land-surface temperature retrieval from ASTER data*. IEEE Geoscience and Remote Sensing Letters, vol. 7(1), 2009, pp. 176–179. https://doi.org/10.1109/LGRS.2009.2029534.

[9] McMillin L.M.: *Estimation of sea surface temperatures from two infrared window measurements with different absorption*. Journal of Geophysical Research, vol. 80(36), 1975, pp. 5113–5117. https://doi.org/10.1029/JC080i036p05113.

[10] Price J.C.: *Land surface temperature measurements from the split window channels of the NOAA 7 Advanced Very High Resolution Radiometer*. Journal of Geophysical Research: Atmospheres, vol. 89(D5), 1984, pp. 7231–7237. https://doi.org/10.1029/JD089iD05p07231.

[11] Morsy S., Hadi M.: *Impact of land use/land cover on land surface temperature and its relationship with spectral indices in Dakahlia Governorate, Egypt*. International Journal of Engineering and Geosciences, vol. 7(3), 2022, pp. 272–282. https://doi.org/10.26833/ijeg.978961.

[12] Wang M., Zhang Z., Hu T., Liu X.: *A practical single-channel algorithm for land surface temperature retrieval: application to Landsat series data*. Journal of Geophysical Research: Atmospheres, vol. 124(1), 2019, pp. 299–316. https://doi.org/10.1029/2018JD029330.

[13] Cristóbal J., Jiménez-Muñoz J.C., Prakash A., Mattar C., Skoković D., Sobrino J.A.: *An improved single-channel method to retrieve land surface temperature from the Landsat-8 thermal band*. Remote Sensing, vol. 10(3), 2018, 431. https://doi.org/10.3390/rs10030431.

[14] Pal S., Ziaul S.K.: *Detection of land use and land cover change and land surface temperature in English Bazar urban centre*. The Egyptian Journal of Remote Sensing and Space Science, vol. 20(1), 2017, pp. 125–145. https://doi.org/10.1016/j.ejrs.2016.11.003.

[15] Tran D.X., Pla F., Latorre-Carmona P., Myint S.W., Caetano M., Kieu H.V.: *Characterizing the relationship between land use land cover change and land surface temperature*. ISPRS Journal of Photogrammetry and Remote Sensing, vol. 124, 2017, pp. 119–132. https://doi.org/10.1016/j.isprsjprs.2017.01.001.

[16] Hidalgo-García D., Arco-Díaz J.: *Modeling the Surface Urban Heat Island (SUHI) to study of its relationship with variations in the thermal field and with the indices of land use in the metropolitan area of Granada (Spain)*. Sustainable Cities and Society, vol. 87, 2022, 104166. https://doi.org/10.1016/j.scs.2022.104166.

[17] Ahmed S.: *Assessment of urban heat islands and impact of climate change on socioeconomic over Suez Governorate using remote sensing and GIS techniques*. The Egyptian Journal of Remote Sensing and Space Science, vol. 21(1), 2018, pp. 15–25. https://doi.org/10.1016/j.ejrs.2017.08.001.

[18] Al-Ruzouq R., Shanableh A., Khalil M.A., Zeiada W., Hamad K., Abu Dabous S., Gibril M.B.A. et al.: *Spatial and temporal inversion of land surface temperature along coastal cities in Arid Regions*. Remote Sensing, vol. 14(8), 2022, 1893. https://doi.org/10.3390/rs14081893.

[19] Majumder A., Setia R., Kingra P.K., Sembhi H., Singh S.P., Pateriya B.: *Estimation of land surface temperature using different retrieval methods for studying the spatiotemporal variations of surface urban heat and cold islands in Indian Punjab*. Environment, Development and Sustainability, vol. 23(11), 2021, pp. 15921–15942. https://doi.org/10.1007/s10668-021-01321-3.

[20] Amindin A., Pouyan S., Pourghasemi H.R., Yousefi S., Tiefenbacher J.P.: *Spatial and temporal analysis of urban heat island using Landsat satellite images*. Environmental Science and Pollution Research, vol. 28(30), 2021, pp. 41439–41450. https://doi.org/10.1007/s11356-021-13693-0.

[21] Sobrino J.A., Jiménez-Muñoz J.C., Paolini L.: *Land surface temperature retrieval from LANDSAT TM 5*. Remote Sensing of Environment, vol. 90(4), 2004, pp. 434–440. https://doi.org/10.1016/j.rse.2004.02.003.

[22] Avdan U., Jovanovska G.: *Algorithm for automated mapping of land surface temperature using LANDSAT 8 satellite data*. Journal of Sensors, vol. 2016, 2016, 1480307. https://doi.org/10.1155/2016/1480307.

[23] Rouse J.W., Haas R.H., Schell J.A., Deering D.W.: *Monitoring vegetation systems in the Great Plains with ERTS*. [in:] Freden S.C., Mercanti E.P., Becker M.A. (eds.), *Third Earth Resources Technology Satellite-1 Symposium. Volume 1: Technical Presentations, section A*, NASA Special Publication, vol. 351, National Aeronautics and Space Administration, Washington 1974, pp. 309–317.

[24] Poveda G., Salazar L.F.: *Annual and interannual (ENSO) variability of spatial scaling properties of a vegetation index (NDVI) in Amazonia*. Remote Sensing of Environment, vol. 93(3), 2004, pp. 391–401. https://doi.org/10.1016/j.rse.2004.08.001.

[25] Ahmad A., Quegan S.: *Analysis of maximum likelihood classification on multispectral data*. Applied Mathematical Sciences, vol. 6(129), 2012, pp. 6425–6436.

[26] Yu K., Chen Y., Wang D., Chen Z., Gong A., Li J.: *Study of the seasonal effect of building shadows on urban land surface temperatures based on remote sensing data*. Remote Sensing, vol. 11(5), 2019, 497. https://doi.org/10.3390/rs11050497.

[27] Meng Q., Liu W., Zhang L., Allam M., Bi Y., Hu X., Gao J. et al.: *Relationships between land surface temperatures and neighboring environment in highly urbanized areas: Seasonal and scale effects analyses of Beijing, China*. Remote Sensing, vol. 14(17), 2022, 4340. https://doi.org/10.3390/rs14174340.